

Attribution-NonCommercial-NoDerivatives 4.0 International (CC BY-NC-ND 4.0)

<https://creativecommons.org/licenses/by-nc-nd/4.0/>

Access to this work was provided by the University of Maryland, Baltimore County (UMBC) ScholarWorks@UMBC digital repository on the Maryland Shared Open Access (MD-SOAR) platform.

Please provide feedback

Please support the ScholarWorks@UMBC repository by emailing scholarworks-group@umbc.edu and telling us what having access to this work means to you and why it's important to you. Thank you.

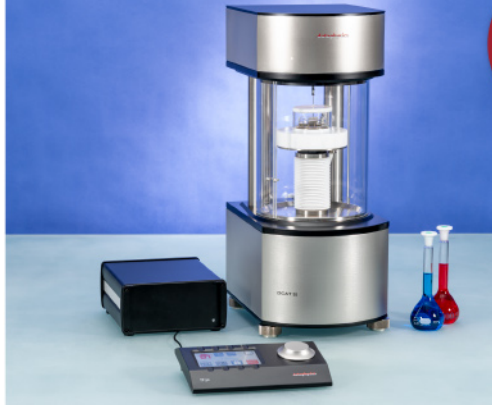


force tensiometry,
dynamic contact angle
measurements, and force
of adhesion evaluation



ASTM D5946
ASTM D7334
ASTM D7490
ISO 27448

optical contact angle
measurements and
drop contour analysis to
determine surface energy
as well as interfacial and
surface tension



ASTM D1331
ASTM D1417
ISO 1409

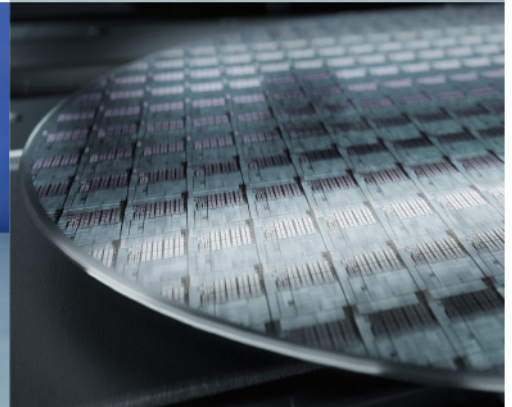


ISO/TR 13097

optical turbidity, stability
and aging analysis of
multi-phase dispersions



zeta potential
measurements
of fibres, powders, and
plate-shaped solids



High-end, versatile laboratory
measurement device portfolio
for a comprehensive analysis of
surfaces and interfaces

Learn more >

dataphysics
Understanding Interfaces

DataPhysics Instruments GmbH
Raiffeisenstraße 34 • 70794 Filderstadt, Germany
phone +49 (0)711 770556-0 • fax +49 (0)711 770556-99
sales@dataphysics-instruments.com
www.dataphysics-instruments.com

Nucleotide-Driven Molecular Sensing of Monkeypox Virus Through Hierarchical Self-Assembly of 2D Hafnium Disulfide Nanoplatelets and Gold Nanospheres

Parikshit Moitra, Maria Iftesum, David Skrodzki, Priyanka Paul, Elnaz Sheikh, Jennifer Lynn Gray, Ketan Dighe, Zach Sheffield, Manas Ranjan Gartia, and Dipanjan Pan*

Liquid interfaces facilitate the organization of nanometer-scale biomaterials with plasmonic properties suitable for molecular diagnostics. Using hierarchical assemblage of 2D hafnium disulfide nanoplatelets and zero-dimensional spherical gold nanoparticles, the design of a multifunctional material is reported. When the target analyte is present, the nanocomposites' self-assembling pattern changes, altering their plasmonic response. Using monkeypox virus (MPXV) as an example, the findings reveal that adding genomic DNA to the nanocomposite surface increases the agglomeration between gold nanoparticles and decreases the π -stacking distance between hafnium disulfide nanoplatelets. Further, this self-assembled nanomaterial is found to have minimal cross-reactivity toward other pathogens and a limit of detection of $7.6 \text{ pg } \mu\text{L}^{-1}$ (i.e., $3.57 \times 10^4 \text{ copies } \mu\text{L}^{-1}$) toward MPXV. Overall, this study helped to gain a better understanding of the genomic organization of MPXV to chemically design and develop targeted nucleotides. The study has been validated by UV-vis spectroscopy, X-ray diffraction, scanning transmission electron microscopy, surface-enhanced Raman microscopy and electromagnetic simulation studies. To the best knowledge, this is the first study in literature reporting selective molecular detection of MPXV within a few minutes and without the use of any high-end instrumental techniques like polymerase chain reactions.

1. Introduction

In the advent of a pandemic, World Health Organization (WHO) very recently declared the spread of another viral infection by monkeypox as an international emergency pirouetting public health. Dating back to the 1970s, the first human Monkeypox Virus (MPXV) case was identified in the Democratic Republic of Congo and was considered to be endemic only in Nigeria and some parts of central and west Africa^[1,2] with the basic reproduction number ranging between 1.10–2.40 in these countries.^[3] However, since early May 2022, MPXV has spread into more than 90 countries and caused >74 K infections across the world with approximately one-third of the cases identified only in the United States.^[4] In this scenario, WHO issued an emergency public health alert on July 23, 2022, which establishes the urgent need for rapid diagnosis of MPXV and immediate isolation of the infected individuals to avoid further community spread.^[5]

P. Moitra, D. Pan
Department of Nuclear Engineering
The Pennsylvania State University
University Park, PA 16802, USA
E-mail: dipanjan@psu.edu

P. Moitra, D. Skrodzki, P. Paul, K. Dighe, Z. Sheffield, D. Pan
Department of Pediatrics
Centre of Blood Oxygen Transport & Hemostasis
University of Maryland Baltimore School of Medicine
Baltimore, MD 21201, USA



The ORCID identification number(s) for the author(s) of this article can be found under <https://doi.org/10.1002/adfm.202212569>.

© 2023 The Authors. Advanced Functional Materials published by Wiley-VCH GmbH. This is an open access article under the terms of the Creative Commons Attribution-NonCommercial-NoDerivs License, which permits use and distribution in any medium, provided the original work is properly cited, the use is non-commercial and no modifications or adaptations are made.

M. Iftesum, E. Sheikh, M. R. Gartia
3261 Patrick F Taylor Hall
Department of Mechanical & Industrial Engineering
Louisiana State University
Baton Rouge, LA 70803, USA

D. Skrodzki, J. L. Gray, D. Pan
Department of Materials Science and Engineering
The Pennsylvania State University
University Park, PA 16802, USA

K. Dighe, Z. Sheffield, D. Pan
Department of Chemical & Biochemical Engineering
University of Maryland Baltimore County
Baltimore County, MD 21250, USA

K. Dighe, D. Pan
Department of Biomedical Engineering
The Pennsylvania State University
University Park, PA 16802, USA

DOI: 10.1002/adfm.202212569

Monkeypox is a zoonotic virus belonging to the Orthopoxvirus genus of the Poxviridae family having an enveloped double-stranded DNA.^[6] Current studies indicate that sexual exposure and close contact are the primary transmission pathways for MPXV.^[7] MPXV is usually detected by performing standard polymerase chain reactions (PCR) on swabs taken from the lesion, the oropharynx and anal mucosa presumably containing higher levels of viral load. PCR is the only available FDA-approved test known for MPXV despite its limitations of complex sample collection, transportation, and insufficient access to advanced instrumental facilities.^[8,9] Serological tests can be thought of as a possible alternative. Since MPXV and Orthopoxvirus have high serological cross-reactivity, antigen- and antibody-based detection methods cannot confirm MPXV infection. Serological and immunological detection methods are therefore not recommended for MPXV diagnosis even where resources are limited for PCR analyses.^[10,11] Moreover, to contain the spread of the disease, an antiviral agent, namely tecovirimat, has recently been approved by the European Medicines Agency (EMA) in 2022.^[12] A modified attenuated vaccinia virus (Ankara strain) has also been approved for the prevention of MPXV.^[13,14] In the current situation, however, both drugs and two-dose vaccines remain insufficient, leaving the only option for disease containment to be rapid diagnosis of MPXV.

Our goal here is to gain fundamental understanding of the genetically preserved regions of the Monkeypox virus, so that highly selective DNA probes can be developed for geno-sensing. Numerous novel approaches are currently being investigated for the process of self-assembling nanoparticles.^[15–19] However, the synthesis of unique multifunctional materials through the hierarchical assemblage of nanoparticles is challenging. Nanostructures can self-assemble or interact at fluid interfaces to generate new or improved properties.^[20] A variety of new approaches are being investigated to develop self-assembled systems on various scaffolds.^[21–28] The unique organization of nanometer-scale materials may offer enhanced plasmonic properties suitable for molecular diagnostics. Nanoparticles can self-assemble at interfaces due to their ubiquitous appearance and occurrence.^[29] On the other hand, heterostructures of 2D nanomaterials can be used for a variety of nanoscale optoelectronic applications.^[30,31] Adding zero-dimensional (0D) plasmonic nanostructures to these 2D materials enhances their spectral properties.^[32–34] Plasmonic nanoparticles have, however, largely been integrated with 2D materials primarily through lithography and/or undefined metallic deposition.^[35] We are using 2D and 0D nanomaterials as building blocks to develop advanced functional materials with improved plasmonic properties. Optical response of host materials can be plasmonically controlled by gold nanostructure integration.

Using hierarchical assemblage of 2D hafnium disulfide nanoplatelets and 0D spherical gold nanoparticles, we herein report the design of a multifunctional material suitable for detecting trace amount of genetic materials in biological samples. We anticipated that unique optical properties may emerge from assembled gold nanoparticles that will differ from their intrinsic forms.^[36] Due to multiple scattering, a plurality of noble metallic nanostructures in close proximity can interact and form new hybrid modes with higher order interactions.^[37,38]

Such properties would potentially be effective for harnessing much-desired sensitivity for molecular detection of low amount of pathogens in biological media. The approach presented here is a simple solution-phase method for 2D/0D heterostructures assembly with enhanced plasmonic properties by using hafnium nanoplatelets to deterministically assemble with AuNPs. Two of the single-strand oligonucleotide sequences targeting complementary MPXV strands were further conjugated to the gold nanoparticles. In presence of its target analyte, the self-assembling pattern of the nanocomposites would be affected, causing a change in plasmonic response. Our results showed that when the genomic DNA of MPXV was added to the surface of the targeted nanocomposite, agglomeration between gold nanoparticles increased and the π -stacking distance between hafnium nanoplatelets decreased. In this way, the nanocomposite showed a significant change in plasmonic response to MPXV with minimal interference from other pathogenic genomic materials (Figure 1).

2. Results and Discussion

2.1. Unique Plasmon Signature from 0D–2D Nanocomposite Material

As evidenced by us and others, the plasmonic response of spherical gold nanoparticles can generally be found around ≈ 520 nm, which selectively shifts toward the red wavelength region after its binding with the target molecule demonstrating a plasmonic response.^[30,39–48] Hence, we combined both 0D spherical nanoparticles with 2D nanomaterials and constructing a heterostructure that can hybridize the complementary advantages of both the platforms and overcome their individual shortcomings.^[49,50] It was envisaged that the synergistic effect of both the 2D and 0D nanomaterials would greatly enhance the sensing performance of the fabricated platform.^[51] Further, it is known that composite materials are able to effectively reduce the working temperature.^[52] Consequently, the composite material has an additional advantage of expected optimum sensing performance at room temperature rather than at 65 °C, which may be required to uncoil the folded double strands of target DNA molecules.^[41] Further, the spatial arrangement of plasmonic nanoparticles can significantly influence their interaction with electromagnetic waves, which offers a systematic method for controlling their optical properties.^[53,54] As a result, significant efforts have been made to develop methodologies that enable high-precision control of the assembly structure of metal nanoparticles. Here we systematically study hierarchical assembly of citrate-stabilized spherical gold nanoparticles with different 2D platforms. These 2D materials include graphene oxide (GO), reduced graphene oxide (rGO), hafnium disulfide (HfS₂) and molybdenum disulfide (MoS₂) nanoplatelet, model covalent organic framework (COF) and copper embedded COF (CuCOF) (Figure 2a). The syntheses of these 2D materials are detailed in the experimental method section. We deliberated about the choice of 2D materials. Although the selected 2D materials have increased surface areas, their chemical backbones differ from one another. Both GO and rGO are known to have carbonaceous backbones, while COF has nitrogen

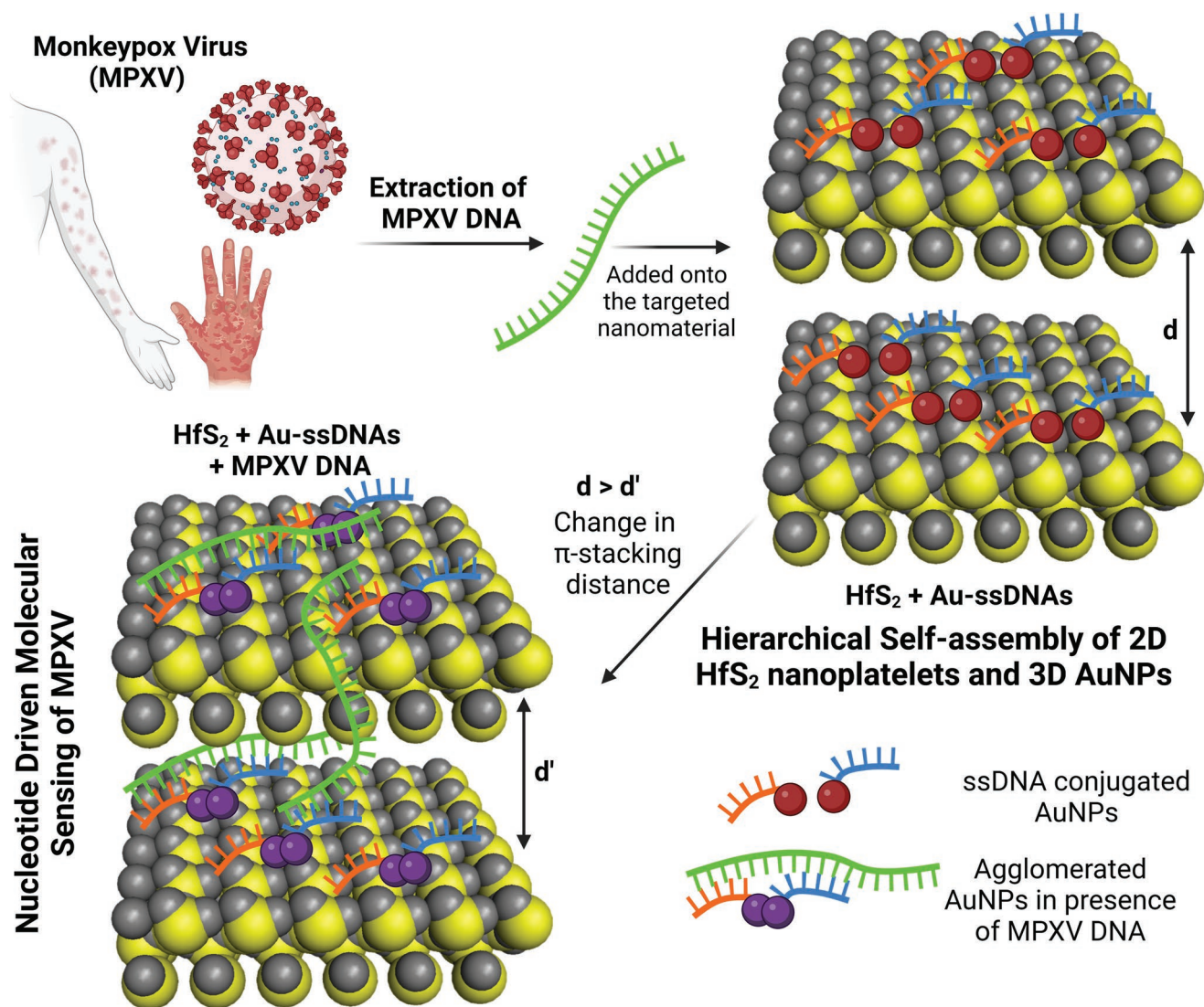


Figure 1. Schematic diagram toward the selective molecular diagnosis of monkeypox virus (MPXV) through hierarchical self-assembly of hafnium disulfide nanoplatelets and nucleotide decorated gold nanoparticles. A significant increase in agglomeration between gold nanoparticles was observed only when MPXV DNA is present and is mediated by complementary DNA sequence targeting. The plasmonic response was further improved due to the H-type aggregation among the hafnium disulfide nanoplatelets leading to a decrease in π -stacking distance.

functionality. CuCOF, on the other hand, has a representative metal functionality included with COF features. HfS₂ and MoS₂ are metal chalcogenides and are known to mimic the properties of GO. Moreover, we expect to have some additional binding between gold nanoparticles and the free sulfur moieties available with HfS₂ and MoS₂ nanoplatelets influencing the aggregation of the nanoparticles.

Now, in order to investigate the aggregation properties of the nanomaterials, a fixed concentration (0.4 mg mL⁻¹) of the 2D nanoplateforms was added to a definite concentration of citrate stabilized AuNPs ($\approx 1.2 \times 10^9$ particles mL⁻¹). It was observed that the addition of COF had no influence on the plasmonic signal of AuNPs. The addition of CuCOF and MoS₂ nanoplatelets only increased the absorbance of AuNPs with no change in wavelength maxima. A clear distinct shift in wavelength was only visible upon the addition of GO, and HfS₂ nanoplateforms

into the suspension of AuNPs (Figure 2b). The wavelength maxima shifted beyond 750 nm with the addition of GO, and there was a ≈ 25 nm bathochromic shift with the addition of HfS₂ nanoplatelets into the suspension of AuNPs. The platform will be negatively affected by the agglomeration of nanoparticles when GO is added, as it will be difficult to observe any further changes in the wavelength maxima that might occur when the target analyte is added. Moreover, HfS₂ has lower optical losses compared to other 2D materials such as graphene and MoS₂ in the visible wavelength region. For example, the complex refractive index of different materials in the form $n^* = n + i k$, are as follows:

$$\begin{aligned} (n^*)_{\text{HfS}_2} &= 3.00 - 0.06i; (n^*)_{\text{MoS}_2} = 5.211 - 1.128i \\ \text{and } (n^*)_{\text{graphene}} &= 2.6 - 1.3i \end{aligned} \quad (1)$$

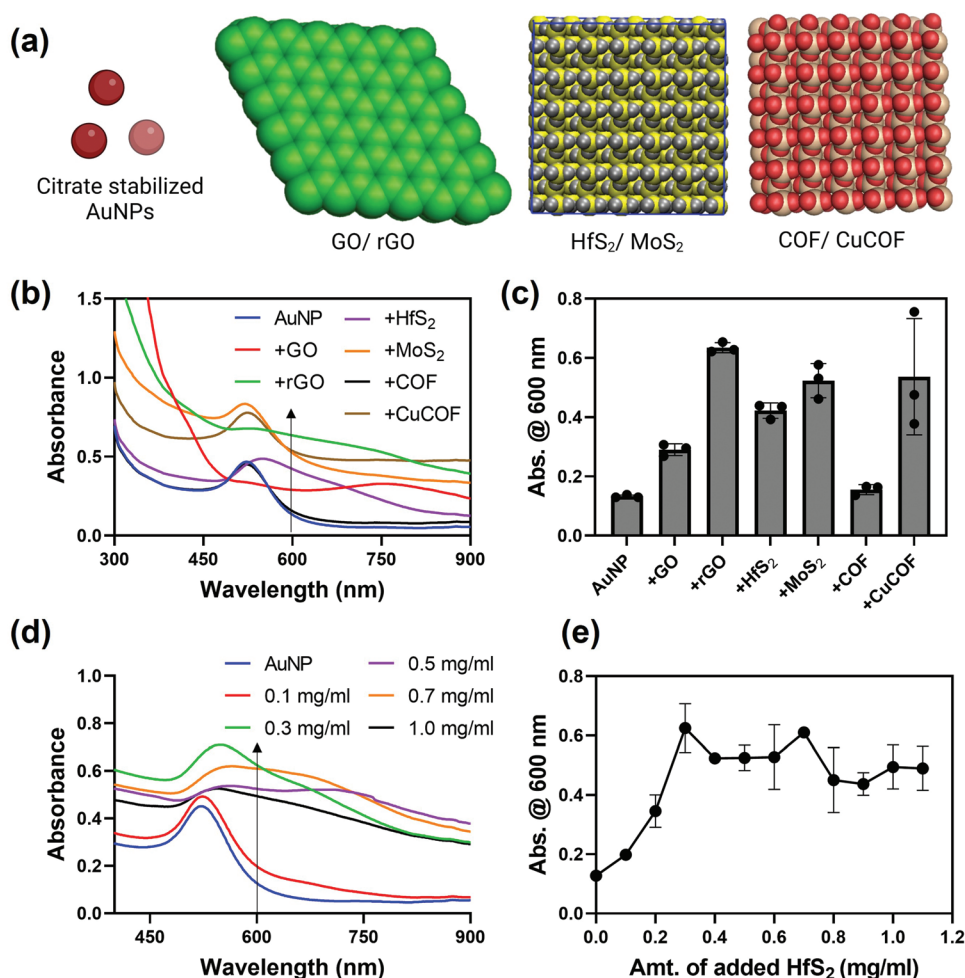


Figure 2. a) Structural backbone of the molecules used in the current study: citrate stabilized gold nanoparticles (AuNPs), GO, rGO, HfS₂, MoS₂, COF, and CuCOF; b) Absorbance and c) Change in absorbance at 600 nm for AuNPs added with equivalent concentration (0.4 mg mL⁻¹) of other nanomaterials; d) Absorbance and e) Change in absorbance at 600 nm for AuNPs added with increasing concentration of HfS₂ nanoplatelets.

Smaller the k value, lower the optical absorption. This could mean less optical loss in case of HfS₂ than other 2D substrates. As such, we decided to proceed with the blend of HfS₂ nanoplatelets and AuNPs where the shift was optimal and further aggregation among the nanoparticles could be observed upon the addition of their target analyte (Figure 2c). However, to confirm that the change in absorbance is caused by the aggregation of the AuNPs rather than due to the optical property of the HfS₂ nanoplatelets, absorption spectra for the HfS₂ nanoplatelet alone (Figure S1, Supporting Information) was also recorded. HfS₂ nanoplatelet suspension has no plasmon peak on its own, but it produces more scattering when used in conjunction with other materials. For optimum aggregation with AuNPs, we titrated the amount of HfS₂ nanoplatelet required. Toward this, an increasing concentration of HfS₂ nanoplatelets was added to the AuNPs (Figure 2d). It was observed that when added sequentially, 0.3 mg mL⁻¹ (1.24 mM) of HfS₂ nanoplatelet was enough to induce agglomeration among citrate stabilized AuNPs (Figure 2e).

To verify the observed experiment results, a finite-difference-time-domain (FDTD) method has been employed to calculate

the electromagnetic field enhancement distributions and justify the use of 2D materials as a composite with 0D particles instead of 0D particles alone. Hence, to model the aggregation of gold nanoparticles in presence of the target DNA, we undertook either a single AuNP or three closely spaced AuNPs. Further to understand the influence of 2D materials, these nanoparticles were either suspended in air or positioned above a substrate mimicking HfS₂ platelet. FDTD results of the gold nanoparticles positioned on the HfS₂ substrate are shown in Figure 3. Figure 3b–d,f–h presents cross-sectional distribution of the normalized EM-field intensity ($|E|^2/|E_0|^2$) of three and a single gold nanoparticle respectively placed over the HfS₂ substrate in the XY, XZ, and YZ planes. These views were compared to the 3 AuNPs (Figure 3a) and 1 AuNP (Figure 3e) alone in the XY plane. Notably, the maximum EM-field enhancement occurs at the junction of the 3 AuNPs and HfS₂ substrate, which is along the XZ plane (red region in Figure 3c) or YZ plane (red region in Figure 3d). These results offer theoretical demonstration that the agglomerated AuNPs decorated on HfS₂ substrate features superior EM-field enhancement, well consistent with the above experiment data. The trimeric AuNPs presented on

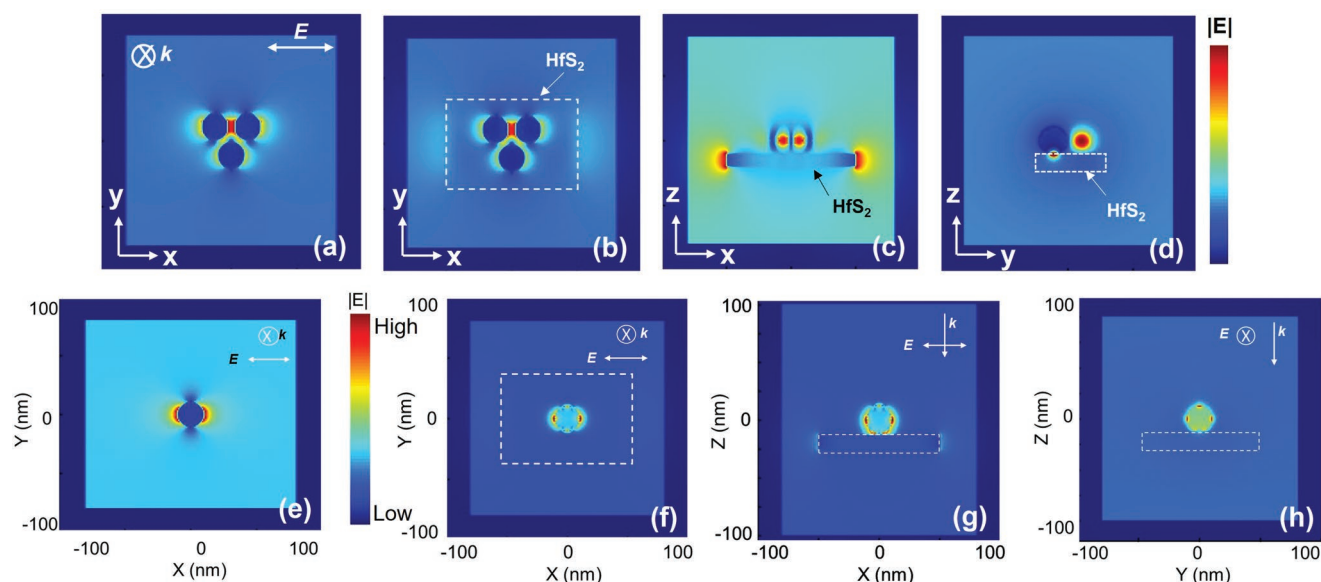


Figure 3. Electromagnetic FDTD simulations of the EM-field intensity distribution for representative a–d) three and e–h) one AuNP in different dielectric environment, e.g., HfS₂ substrate (b–d and f–h) and air (a and e). Cross-section views for calculating the EM-field enhancement distribution of gold nanoparticles, positioned on the substrate are also shown along XY, XZ, and YZ planes. The region enveloped in white frame represents HfS₂ in the simulations. The colors from blue to red represent the EM-field intensity from weak to strong. $|E|^2$ and $|E_0|^2$ stand for scattered EM-field intensity and incident EM-field intensity respectively. The incident EM-field was polarized in X-direction and propagation vector (k) was in Z-direction.

HfS₂ increased the electric field, $|E|$, by a factor of $\approx 10\times$, compared to single nanoparticle. The increased EM-field also contributed to $\approx 10\times$ increase in scattering cross-section, which will lead to scattering of more photons. Increased scattering cross-section is advantageous for colorimetric (UV–vis absorbance based) detection. HfS₂ provides a “nano/micro” substrate for the AuNP to form dimer/trimer/multi-NP (aggregated) structures. This increases the electromagnetic (EM) field at the gap between the AuNPs. The increased EM field or the so-called “hot spots” lead to enhanced light-matter interactions between incident light and the targeted bio-analyte. In addition, HfS₂ increased the density of AuNP per unit incident light beam area without aggregation (Figure 3f–h) when compared to the single AuNP in air (Figure 3e). This improves the absorption coefficient. Further in the presence of HfS₂, the plasmonic field gets enhanced and extended both in x and z direction (Figure S2, Supporting Information). Thus, it may be concluded that this enhanced light-matter interaction, introduced by the 0D+2D composite material than the 0D particles alone, will lead to significant improvement in sensitivity.

Now, to visualize the maximum change in absorbance for the composite material with the addition of its target MPXV DNA, we closely observed their absorption peak as obtained in Figure 2b. The absorption graph obtained with the addition of HfS₂ platelets to the suspension of Au nanoparticles were shown separately in Figure S3a (Supporting Information). The spectrum of the composite was then analyzed where we observed that two separate peaks were contributing to the absorbance spectra for the composite (Figure S3b, Supporting Information). The theoretically predicted UV spectra also supported the fact. The increase in scattering cross-section by orders of magnitude was due to the involvement of HfS₂

(Figure S3c, Supporting Information). The improved scattering cross-section may lead to better colorimetric detection. Two separate positioned peaks, 536 and 607 nm were found in the composite absorption spectra predicted theoretically (Figure S3d, Supporting Information). The red shift of plasmonic resonance with the involvement of HfS₂ and appearance of new peak at $\lambda = 607$ nm was in corroboration with the experimental data (Figure S3a, Supporting Information). All these data thus support the involvement of 2D materials with 0D particles as a composite than 0D particles alone to obtain better sensitivity toward a selected analyte. Because the composite system offers improved scattering and absorption cross-sections at 540 nm, we decided to monitor the absorbance at 540 nm to determine the material's effectiveness toward MPXV DNA sensing. Also, the change in plasmonic response was the maximum at 540 nm than at 610 nm which helped in determining the optimum ssDNA set and the sensitivity and selectivity of the composite system toward MPXV DNA.

2.2. Design of Newly Targeted Oligonucleotide Sequences

Once the sensing platform is optimized, the next question comes of how to target the platform toward an analyte, i.e., MPXV DNA. We considered Monkeypox viral strain USA_2003_039 and analyzed its genomic organization at this point. Bifunctional hemagglutinin and EEV type-I membrane glycoprotein are the two genomic segments directly related to viral infection progression and are highly conserved across MPXV strains (Figure 4a).^[55,56] Hence, we targeted our study toward these two genetic segments and designed single-stranded oligonucleotides (ssDNAs) based on their target

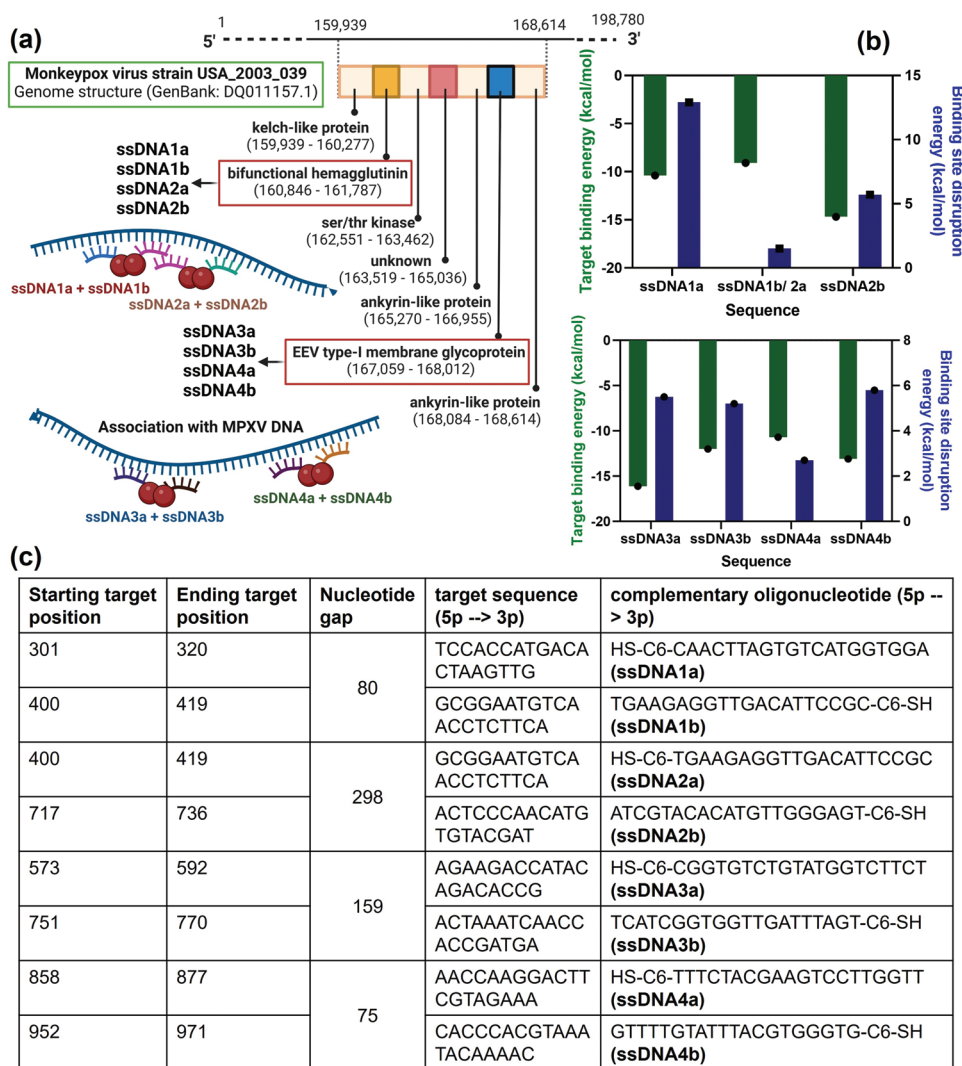


Figure 4. a) Genomic organization of MPXV strain USA_2003_039 and target location of single stranded DNAs (ssDNAs) complementary toward MPXV DNA; b) Comparative target binding energy and binding site disruption energy for the designed ssDNAs; c) Details of designed ssDNAs with their target sequence and nucleotide gap positions.

binding energy and binding site disruption energies (Figure 4b). The ssDNAs were designed in pairs and in such a way that they follow closely spaced target sequences. While ssDNA1 (pair of ssDNA1a and ssDNA1b) and ssDNA2 (pair of ssDNA2a and ssDNA2b) were targeted toward bifunctional hemagglutinin, ssDNA3 (pair of ssDNA3a and ssDNA3b) and ssDNA4 (pair of ssDNA4a and ssDNA4b) were directed toward EEV type-I membrane glycoprotein (Figure 4a). The sequence of these ssDNAs together with their target position and sequence has been tabulated in Figure 4c. While the first partner of the ssDNA pair is thiolated at the 5'-end, the other partner of the ssDNA pair is thiolated at the 3'-end to influence agglomeration among the AuNPs in presence of their target analyte. If the ssDNAs are conjugated to AuNPs, the agglomeration of the AuNPs will be a function of the nucleotide gap between the two ssDNAs. Thus, ssDNA4 should show better aggregation than any other ssDNA (Figure 4c).

2.3. Standardization and Selective Sensing of Monkeypox DNA

2.3.1. Standardization of the Sensing Platform

Accordingly, all the ssDNAs were individually conjugated to the AuNPs and the respective pairs were mixed in equal volumes, i.e., ssDNA1a conjugated AuNPs were mixed with ssDNA1b conjugated AuNPs in equal volume and so on. The respective mixture was then added to the HfS₂ nanoplatelet to monitor their previously determined aggregation proficiency. However, it was seen that upon conjugation of AuNPs with ssDNAs, 0.3 mg mL⁻¹ (1.24 mM) of HfS₂ nanoplatelet was not enough to induce agglomeration. Hence, we re-titrated the amount required for HfS₂ nanoplatelet to initiate aggregation among AuNPs (Figure 5a). It was observed that the required amount of HfS₂ nanoplatelet increased almost 10 times, i.e., 3.0 mg mL⁻¹ (12.4 mM), when its aggregation was considered with AuNPs at

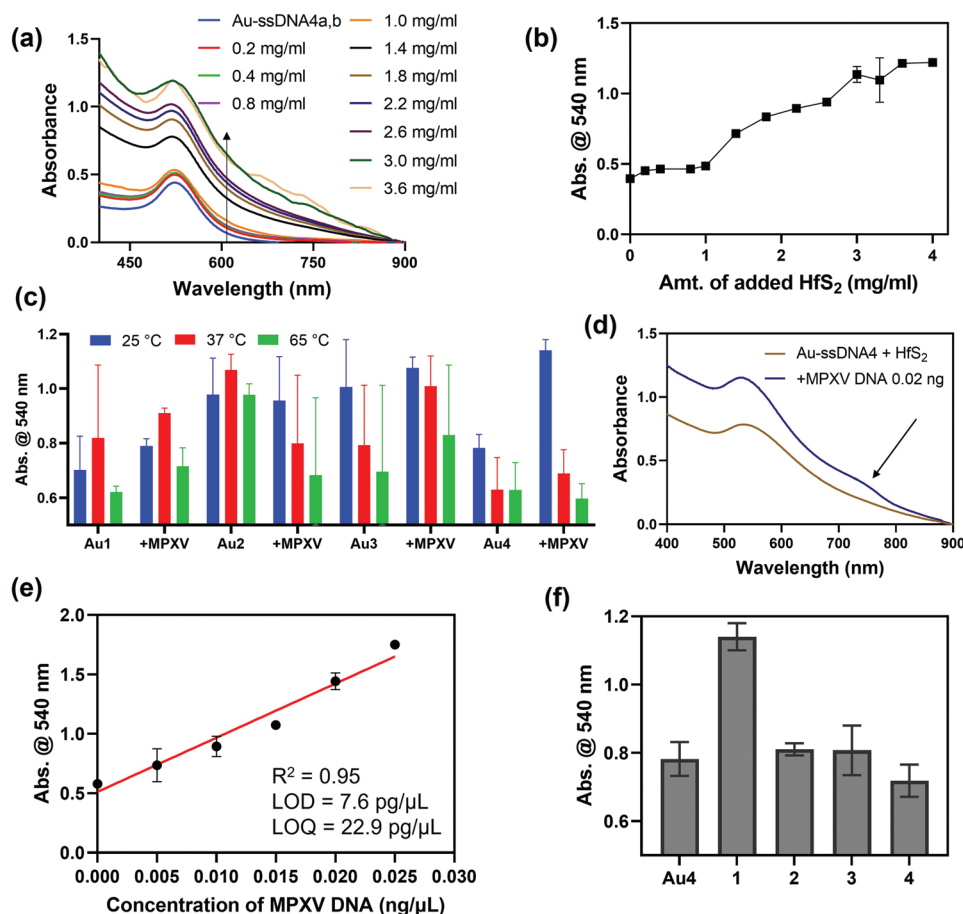


Figure 5. a) UV-vis absorbance and b) Change in absorbance at 540 nm for a mixture of ssDNA4a and ssDNA4b conjugated AuNPs added with increased concentration of HfS₂ nanoplatelets; c) Change in absorbance at 540 nm while the variants of nucleotide decorated AuNPs were added with an equivalent concentration of MPXV DNA (0.02 ng mL⁻¹) and incubated at three different temperatures; Here **Au1** corresponds to a mixture of ssDNA1a and ssDNA1b conjugated AuNPs, **Au2** corresponds to a mixture of ssDNA2a and ssDNA2b conjugated AuNPs, **Au3** corresponds to a mixture of ssDNA3a and ssDNA3b conjugated AuNPs, and **Au4** corresponds to a mixture of ssDNA4a and ssDNA4b conjugated AuNPs; d) UV-vis absorbance of the ssDNA4 decorated AuNPs designed over HfS₂ nanoplatelet before and after the addition of MPXV DNA at 0.02 ng mL⁻¹ concentration; e) Limit of detection (LOD) and limit of quantification (LOQ) toward the detection of MPXV DNA; f) Cross-reactivity of the nano-system toward the selective molecular detection of MPXV; Here **1** is MPXV genomic DNA, **2** and **3** is the genomic DNA of *Chlamydia trachomatis* and *Neisseria gonorrhoeae* respectively and **4** is SARS-CoV-2 genomic RNA.

600 nm (Figure 5b). As a result of this observation, we hypothesized that ssDNA-conjugated AuNPs increased the stacking distance among nanoplatelets compared to citrate-stabilized AuNPs during nanoplatelet aggregation.

2.3.2. Selective Sensing of MPXV DNA

This optimized suspension, i.e., AuNPs admixed with 3 mg mL⁻¹ of HfS₂ nanoplatelets, was then used for the detection of MPXV DNA sequence at three different incubating temperatures. First, the absorbance of the respective mixture of HfS₂ nanoplatelet mixed with equivalent volume of Au-ssDNA_xa and Au-ssDNA_xb was recorded. Here, x indicates the respective number of ssDNA, i.e., 1, 2, 3, or 4. MPXV genomic DNA was then added to the suspension at a fixed concentration of 0.02 ng μL⁻¹, incubated for 10 min either at 25, 37, or 65 °C, and recorded the final change in absorbance. It was found that

Au-ssDNA4 added with HfS₂ nanoplatelet gave the maximum change in absorbance in the presence of MPXV DNA at 25 °C compared to the other pair of ssDNAs conjugated to AuNPs (Figure 5c). An increase in absorbance together with appearance of a charge transfer band at ≈750 nm indicated the association of ssDNA4a and ssDNA4b pair of oligonucleotides with their complementary MPXV strands (Figure 5d). There is also a blue shift of the absorption peak at ≈540 nm after the addition of MPXV DNA which indicates the decrease in π -stacking distance among the self-assembled nanostructures (H-type aggregation).^[57,58] The absorption peak at ≈750 nm may be attributed to the presence of agglomerated Au nanoparticles of higher size.^[47] This observation matched with our hypothesis that upon binding to its target MPXV DNA, the 0D–2D nanocomposite material will shift its plasmon response to a higher wavelength region. It can be imagined that in presence of MPXV DNA, the ssDNAs bind to their complementary strands leading to increased agglomeration among the

AuNPs and decrease in π -stacking distance between the HfS₂ nanoplatelet.

Following this, an increasing concentration of MPXV genomic DNA was added to the suspension of HfS₂ nanoplatelet mixed with ssDNA4a and ssDNA4b conjugated AuNPs. The limit of detection (LOD) of MPXV DNA was calculated to be 7.6 pg μL^{-1} , i.e., 3.57×10^4 copies μL^{-1} (Figure 5e). Further to experimentally validate the importance of 0D+2D composite material toward the efficient sensing of MPXV DNA, another control experiment with 0D Au-ssDNA4 alone in absence of any 2D materials was performed. Increase in absorbance at 540 nm was observed with the increase in MPXV DNA concentration added to the suspension of Au-ssDNA4. However, the increase in absorbance was found to be only 0.0689 with the addition of 0.025 ng μL^{-1} concentration of MPXV DNA (Figure S4, Supporting Information), which is amplified to ≈ 17 times when 2D HfS₂ platelet is added to the sensing media. For the composite material, increase in absorbance of 1.172 at 610 nm was found with the addition of 0.025 ng μL^{-1} concentration of MPXV DNA (Figure 5e). This also proves the importance of the composite material toward the plasmonic sensing of target analyte. Further, this developed system was found to have minimal cross-reactivity with other pathogen-extracted genomic material

establishing the selectivity of the newly designed ssDNA strands toward their target MPXV DNA sequences (Figure 5f).

2.4. Proof from X-Ray Diffraction Studies

This observation was then proved by X-Ray diffraction (XRD) studies. The suspension containing ssDNA4 conjugated AuNPs admixed with HfS₂ nanoplatelets before and after the addition of MPXV DNA was drop casted on a flat silicon surface and examined by XRD. The XRD pattern was also compared with unmodified HfS₂ nanoplatelets. It was observed the XRD peak representing the π -stacking distance among the HfS₂ nanoplatelets shifted toward lower theta angle upon the addition of ssDNA conjugated AuNPs, which further shifted toward higher theta angle with the addition of its target MPXV genomic DNA (Figure 6a). The respective d value was then calculated from the theta angles and the change in π -stacking distance among the nanocomposite materials were monitored (Figure 6b). The XRD data thus validates that there is an increase in π -stacking distance with the addition of ssDNA capped gold nanoparticles on to the surface of HfS₂ nanoplatelet. However, the π -stacking distance decreased upon the addition of target MPXV DNA to

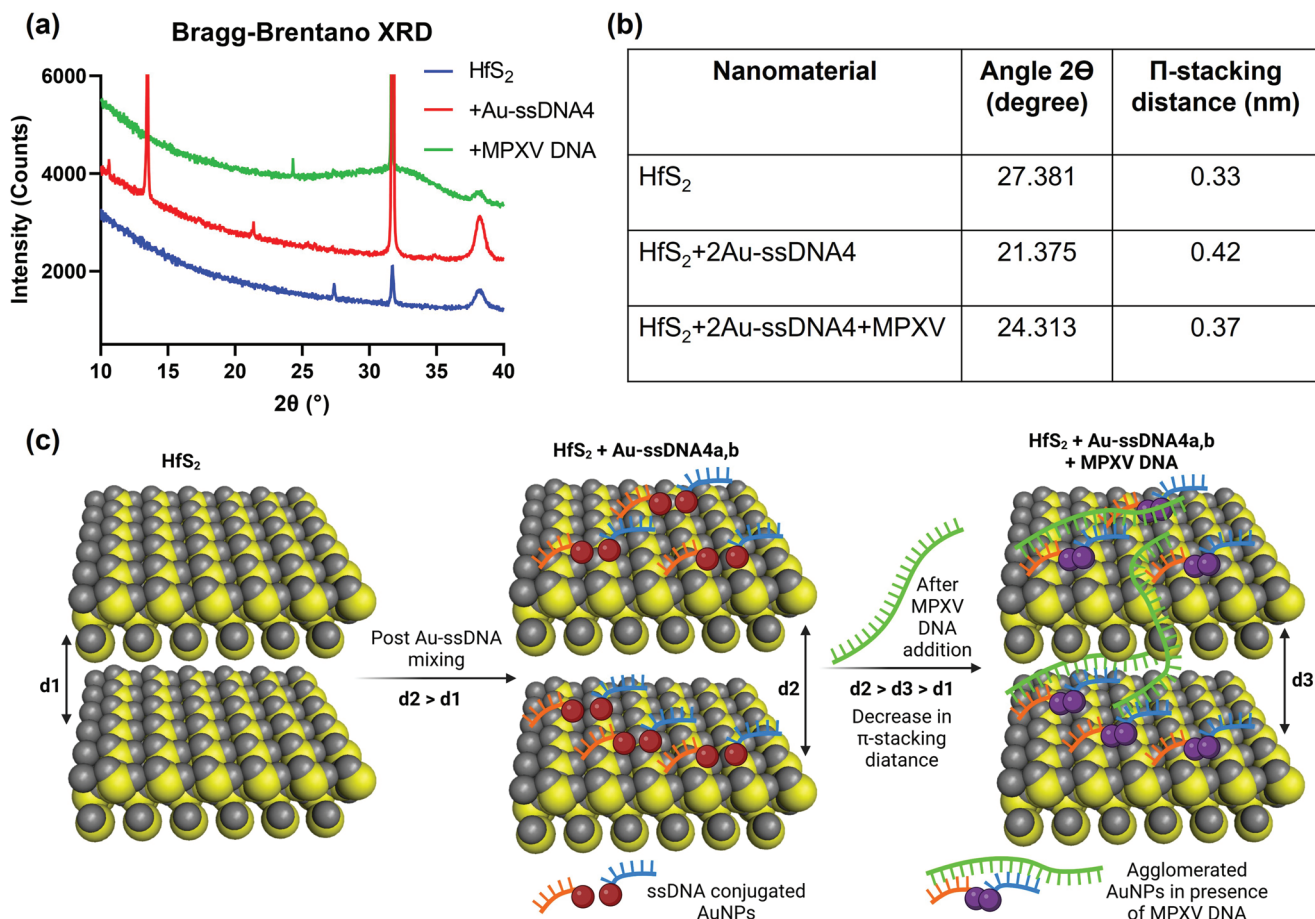


Figure 6. a) X-Ray diffraction pattern of HfS₂ nanoplatelet, ssDNA4a and ssDNA4b conjugated AuNPs mixed with HfS₂ nanoplatelet before and after the addition of MPXV DNA; b) Change in π -stacking distance among the nanocomposite material; c) Schematic diagram of the nano-assembly before and after the addition of MPXV DNA indicating change in π -stacking distance and improved agglomeration among the plasmonic nanoparticles.

the composite material. This phenomenon has been schematically represented in Figure 6c.

2.5. Theoretical Proof of Plasmon Response

Now to explain the combined changes in plasmon response and stacking distance as observed by UV-vis and X-ray diffraction studies, a theoretical calculation was then performed to understand the variation in HOMO-LUMO distance between gold nanoparticles and HfS₂ nanoplatelets. Accordingly, we have first minimized the energy of the complexes and then calculated their HOMO-LUMO distance with B3LYP model in GAMESS software (Figure 7).^[59–61] For easier theoretical calculations, we considered five nucleotide strands instead of twenty nucleotide strands for ssDNAs. These are the first few strands similar to ssDNA4a (Au-TTCT) and ssDNA4b (GGGTG-Au). The target MPXV DNA, considered for theoretical calculation, was of ten nucleotide strands (AGAAACACCC). The HOMO-LUMO distance has been calculated and the results are tabulated in Table S1 (Supporting Information). It was observed that upon addition of equivalent mixture of ssDNA4a and ssDNA4b conjugated AuNPs to the HfS₂ nanoplatelets, the HOMO-LUMO distance decreased. The HOMO-LUMO gap was found to further decrease upon the addition of MPXV DNA to the nanocomposite formulation. This further corroborates our observation in red shift in wavelength especially upon the addition of MPXV DNA.

2.6. Morphological Investigation

Finally, these observations were supported by scanning transmission electron microscopic (STEM) studies which demonstrated the aggregation propensity of the nanomaterials. The surface topography and energy-dispersive (EDS) layered images of the designed nanocomposite material before (Figure 8a–d) and after the addition of MPXV genomic DNA (Figure 8e–h) was observed. The arrangement of ssDNA capped AuNPs were clearly visible over the surface of HfS₂ platelet (Figure 8a) which has been validated from the respective EDS images (Figure 8b–d). The addition of MPXV DNA agglomerated the AuNPs (Figure 8e) and the clustered AuNPs were demonstrated in the respective EDS map (Figure 8f–h). The aggregation phenomenon has been further established while the non-specific DNA from *Neisseria gonorrhoeae* bacteria was added into the nano-assembly of HfS₂+Au-ssDNA4 instead of MPXV DNA. There was no similar agglomeration between AuNPs (Figure 8i–l) was found as observed in case for MPXV DNA, demonstrating the specificity of the system. The respective SEM images were shown in Figures S5 and S6 (Supporting Information). Further, while comparing the respective EDS block images, footprints of aggregated AuNPs could be visualized in presence of MPXV DNA. The presence of C and O was also significantly increased in the presence of the target analyte, as confirmed by EDS (Figure S6, Supporting Information). This is presumably due to the increase in the concentration of C and O and indicative of increased nucleotide concentration on the surface of the composite nanomaterial.

Further, to confirm the reproducibility of the generated structures, it is to be mentioned that the obtained solution phase UV spectra can average out any non-uniform distribution of 0D particles on the 2D material surface. The spectra were collected multiple times by UV-vis spectrophotometer and similar results were obtained each time. Hence, it can be said that the sensing output will remain the same even if there is any uniformity in produced composite material. Further, we have now performed surface-enhanced Raman spectroscopy (SERS) to investigate the composite system in absence and presence of their target MPXV DNA. The enhanced light-matter interaction, as observed for the composite material in comparison to the 0D particles alone (Figure 3; Figures S2 and S3, Supporting Information), influenced us to exploit the system for other detection methodology such as surface-enhanced Raman spectroscopy (SERS). The SERS results combined with machine learning techniques support the reproducibility of the developed composite system toward the selective detection of MPXV DNA with ≈100% accuracy. The agglomeration among the AuNPs in presence of their target analyte will cause a change in surface plasmon resonance and introduce a change in the SERS response. The bright-field images for the composite material alone (Figure 9a) and in presence of the target MPXV DNA (Figure 9c) and non-target *Neisseria gonorrhoeae* (NG) DNA (Figure 9e) has been presented. A large surface area was scanned for each of the samples to monitor the red spots and nanogaps between AuNPs. Multiple Raman spectra were collected for each of the samples and the presented Raman spectra is an average of all the acquired ones (Figure 9h). The red spots were presumably generated due to the hot spots created by the agglomeration of AuNPs over HfS₂ surface. More hot spots were found in case where the composite material was added with target MPXV DNA than the non-target NG DNA (Figure 9b,d,f). These results further support the efficacy of the developed system toward the sensing of MPXV DNA. Principal component analysis (PCA) was also performed on the obtained Raman dataset. The PCA score plot showed a defined separation between the composite material treated with target MPXV and non-target NG DNA (Figure 9g). The Raman peaks were also assigned and presented in Table S2 (Supporting Information).

3. Conclusion

In summary, we have developed a multifunctional material through hierarchical self-assembly of 0D–2D nanostructures targeted toward the genomic DNA of the Monkeypox virus. The use of composite material (2D platelet + 0D particles) has been justified over the use of 0D particles alone by electromagnetic FDTD simulations. New single-stranded oligonucleotide sequences were designed and conjugated to the gold nanoparticles before being used for association with the 2D hafnium nanoplatelet. This nanocomposite material when exposed to the genomic DNA of MPXV demonstrated a decrease in π -stacking distance between the hafnium nanoplatelets and an increase in agglomeration among the nanoparticles. X-ray diffraction, scanning transmission electron microscopy and surface-enhanced Raman microscopy studies have confirmed these findings. We

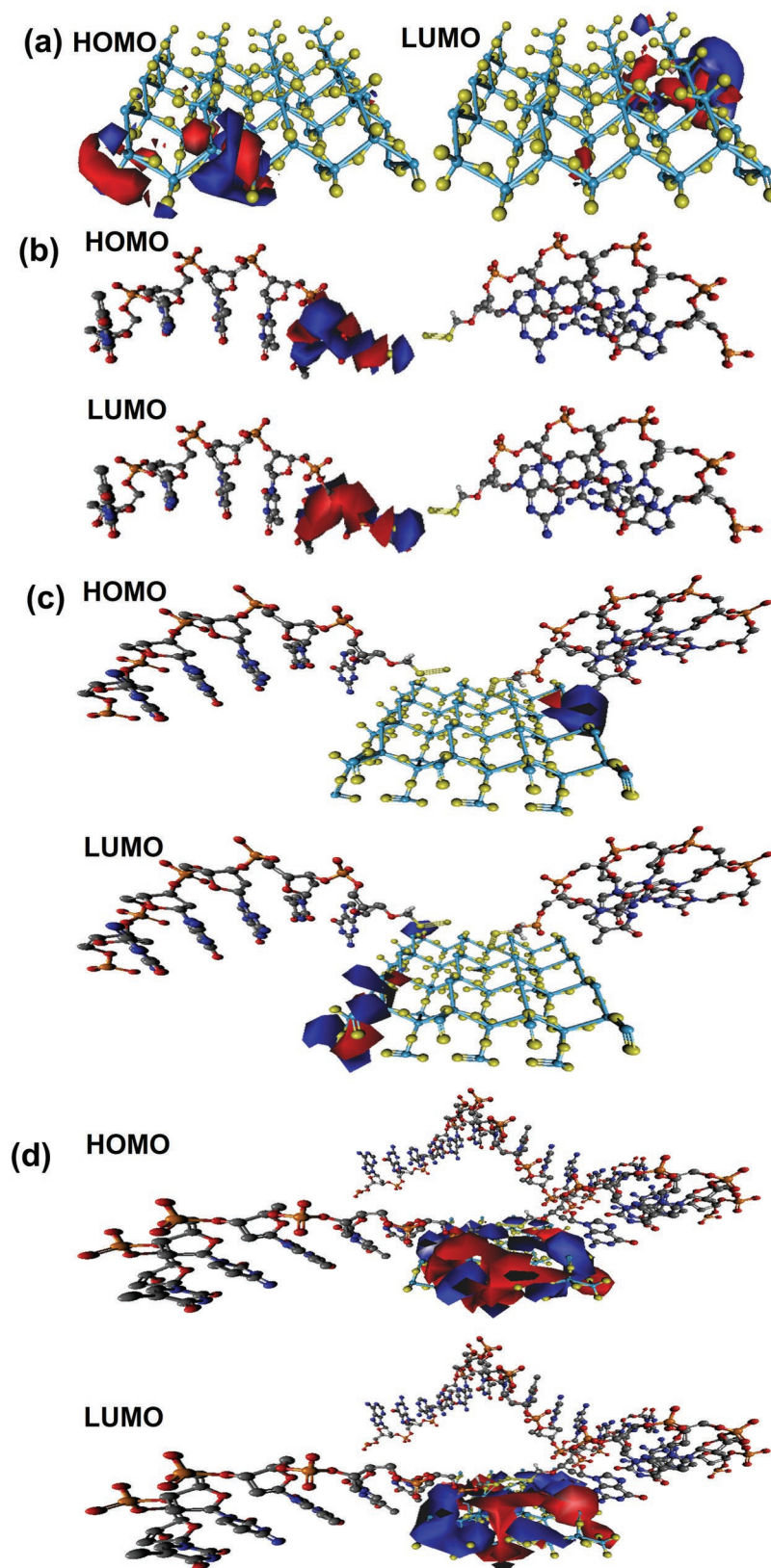


Figure 7. HOMO (top) and LUMO (bottom) representation for the energy minimized structures of a) HfS₂ nanoplatelet; b) ssDNA4a and ssDNA4b conjugated AuNPs; ssDNA4a and ssDNA4b conjugated AuNPs mixed with HfS₂ nanoplatelet c) before and d) after the addition of MPXV DNA. The red and blue colored blobs represent the phase of the molecular orbital, i.e., positive, or negative. While HOMO and LUMO represent the electron donor and electron acceptor regions respectively, the electron-rich or positive values are shown as red and electron-poor or negative values are shown as blue color-coded blobs.

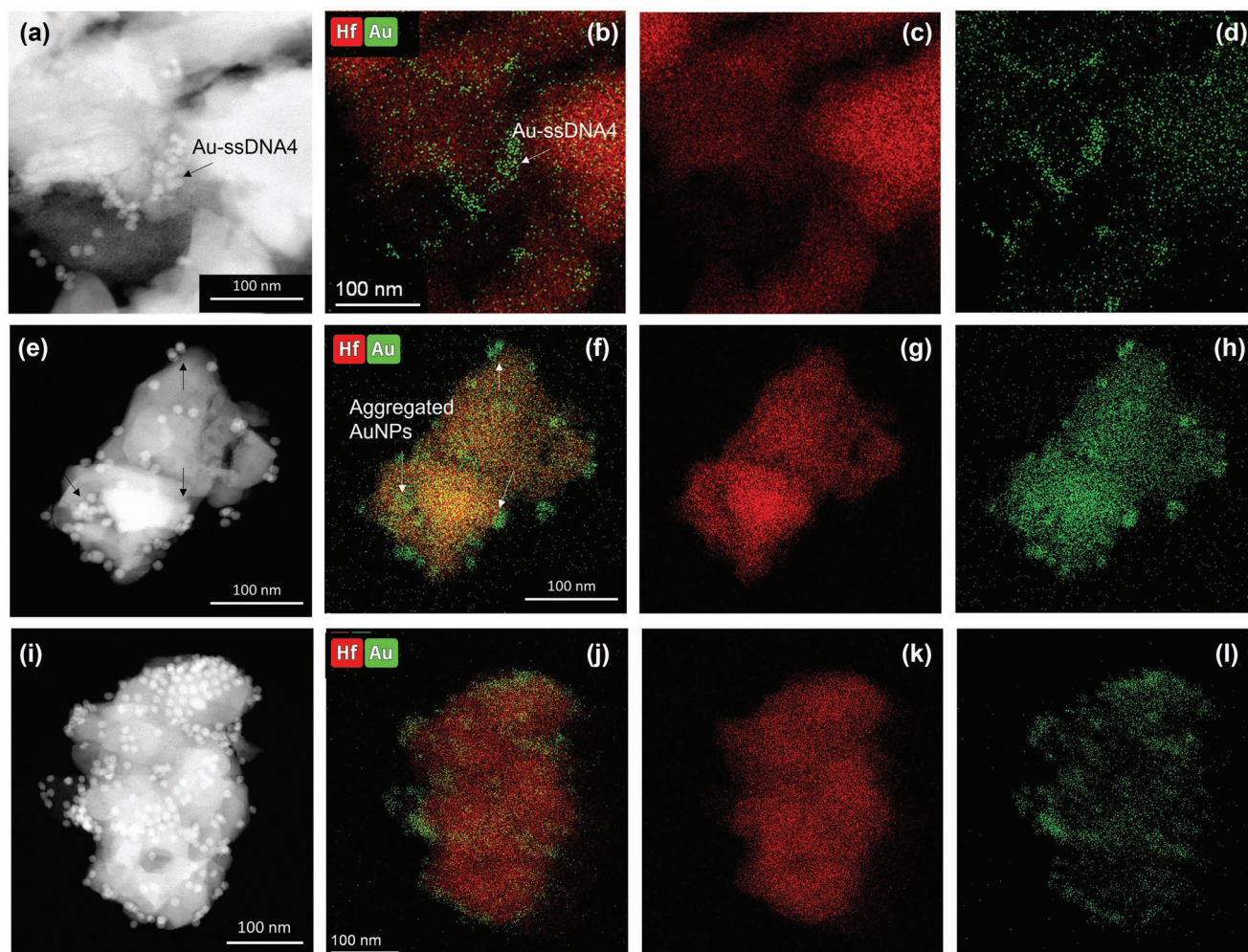


Figure 8. STEM images of the nano-assembly a) before, after the addition of e) MPXV DNA and i) DNA from *Neisseria gonorrhoeae* bacteria at $0.02 \text{ ng } \mu\text{L}^{-1}$ concentration. The agglomeration among the AuNPs was observed from the (b, f, j) overlay EDS images for Hf and Au while the separate EDS maps for Hf and Au were shown in (c, g, k) and (d, h, l) respectively. The red and green color encodes for Hf and Au respectively. The white arrows show the dispersed gold nanoparticles in (b), and the agglomerated gold nanoparticles in (f).

conducted UV-vis spectroscopy to determine whether the nano-material's plasmonic response changed upon adding MPXV DNA. A theoretical calculation of the HOMO-LUMO orbital gap also confirmed the observation. When other pathogen genomic materials were added to the nanomaterial developed for MPXV DNA, a similar change in plasmonic response was not observed, confirming the selectivity of the material. The limit of detection of MPXV DNA for the nanomaterial was also found to be $7.6 \text{ pg } \mu\text{L}^{-1}$, i.e., $3.57 \times 10^4 \text{ copies } \mu\text{L}^{-1}$. We believe that this is the first article in literature to describe a rapid molecular sensing platform that is capable of selectively and sensitively detecting MPXV using a simple absorbance reader without the need for high-end instrumental techniques such as PCR. Using a unique 0D–2D self-assembled hierarchical nanosystem that can sense trace amounts of viral DNA, this study helps us understand how to specifically target and sense a mutationally conserved region of monkeypox virus genome. Moreover, the significance of advanced 0D–2D assemblies toward medical diagnosis of monkeypox virus is also described. Thus, this work may lead to a new technological pathway enabling the diagnosis

of monkeypox virus easily, rapidly, and selectively, preventing it from spreading.

4. Experimental Section

Materials: Chloroauric acid (product code 254169), trisodium citrate (product code S4641), graphite powder (product code 1042062500), hafnium chloride (product code 590592), oleylamine (product code HT-OA100), carbon disulfide (product code 180173), sodium molybdate (product code 737860), thiourea (product code T8656), *p*-phenylenediamine (product code P6001), copper chloride (product code 751944) were purchased from Sigma-Aldrich and were used without any further purification steps.

Design of Complementary ssDNA Strands: The complete genome of monkeypox virus strain USA_2003_039, GenBank: DQ011157.1, was considered and the nucleotide sequences for bifunctional hemagglutinin and EEV type-I membrane glycoprotein were supplied to Soligo software.^[62] The software can perform statistical folding of nucleic acids and predict the most suitable complementary single-stranded oligonucleotide sequence that reflects higher binding energy and optimum binding site disruption energy. The prediction run was carried

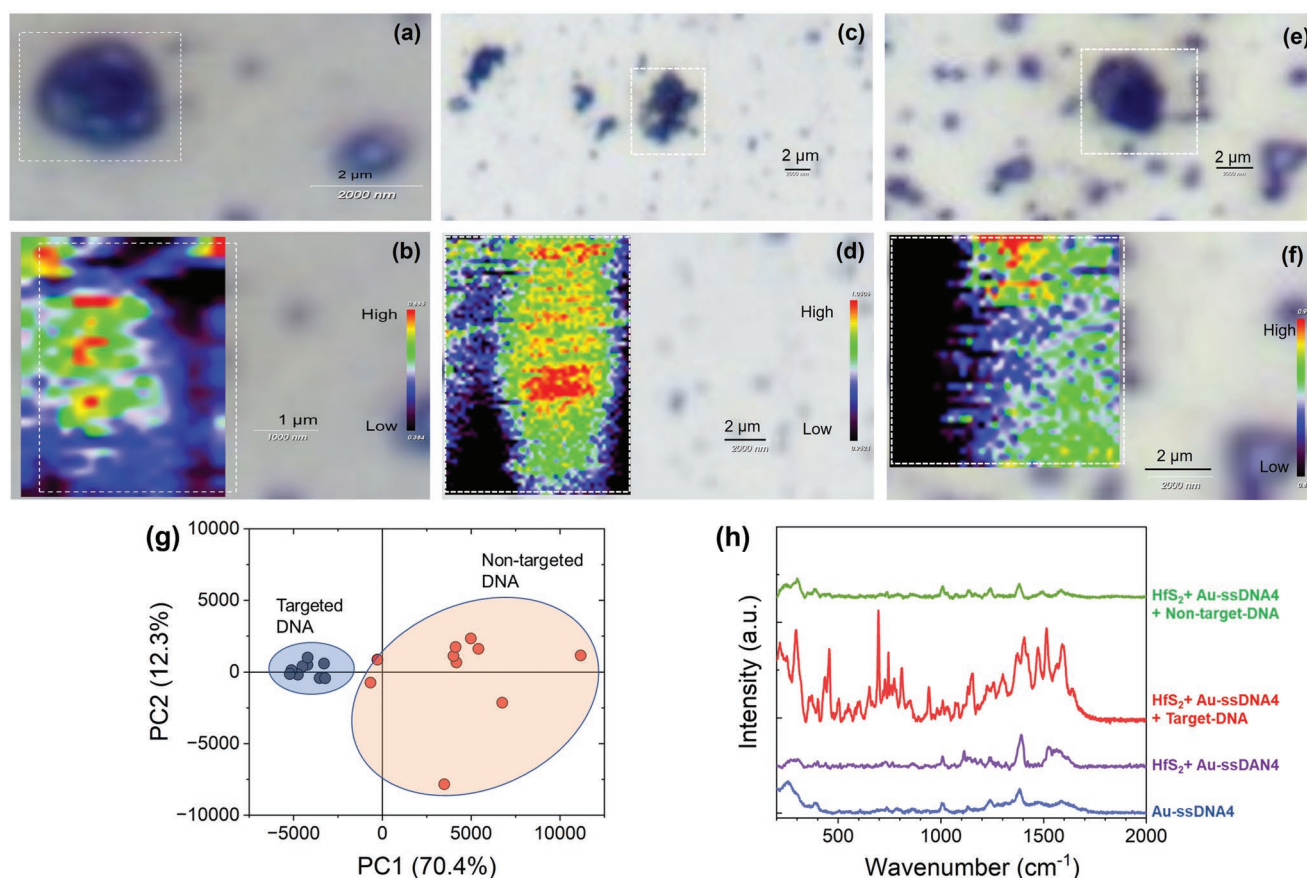


Figure 9. a,c,e) Bright-field and b,d,f) Raman microscopic mapping images of the composite material alone (a, b) and in presence of the target MPXV DNA (c, d) and non-target *Neisseria gonorrhoeae* (NG) DNA (e, f) (785 nm laser, 45 mW (50%) power, grating of 1200, 100 \times magnification, time 0.3 s) with the center of 1100 cm^{-1} . Red means high SERS intensity (indicating the presence of dimer/trimer particles and “hot spot” of EM-field enhancement) and blue indicates lower SERS intensity; g) PCA score plot constructed using the SERS spectra showing the separation between negative and positive samples added to the composite material; h) Representative SERS spectra for the studied materials including ssDNA capped AuNPs, $\text{HfS}_2 + \text{Au-ssDNA4}$ in absence and presence of target MPXV and non-target *Neisseria gonorrhoeae* (NG) DNA.

out maintaining the folding temperature at 37 $^{\circ}\text{C}$ and ionic conditions of 1 M sodium chloride for a preferred length of nucleotide as 20. The output sequences were further studied where the ones closely following each other with optimum binding energy and binding site disruption energy were selected as pairs. The sets of pairs of nucleotides are mentioned below:

ssDNA1a: CAACTAGTGTTCATGGTGA;
ssDNA1b: TGAAGAGGTTGACATTCGGC
ssDNA2a: TGAAGAGGTTGACATTCGGC;
ssDNA2b: ATCGTACACATGTTGGGAGT
ssDNA3a: CGGTGTCTGTATGGTCTTCT;
ssDNA3b: TCATCGGTGGTTGATTTAGT
ssDNA4a: TTTCTACGAAGTCCTTGGTT;
ssDNA4b: GTTTTGATTTACGTGGGTG

All the nucleotide sequences were mentioned as 5' to 3'. ssDNA1a, ssDNA1b, ssDNA2a, and ssDNA2b are targeted toward the bifunctional hemagglutinin sequence of the monkeypox virus, whereas the rest of the ssDNAs are targeted toward EEV type-I membrane glycoprotein. Further to influence the agglomeration efficiency between the pair of nucleotide sequences with their target complementary strands when connected to plasmonic nanoparticles, one set of nucleotides (1a, 2a, 3a, and 4a) were custom synthesized with a thiol functionality at their 5'-end connected to a six-spacer carbon unit. The other sets of nucleotides (1b, 2b, 3b, and 4b) were custom synthesized with a thiol moiety at their 3'-end connected to a six-spacer carbon unit.

Synthesis of Citrate Stabilized Gold Nanoparticles (AuNPs): The synthesis was followed from a previously published literature protocol.^[40,45] Briefly, 20 mL of 1 mM solution of chloroauric acid was heated to boiling under stirring condition. 2 mL of 1% solution of sodium citrate was added to it. The solution was stirred for 10 min under boiling condition and then removed from heating. The color of the solution changed from yellow to wine red color within this time frame. Finally, the solution was centrifuged at 25 000 g for 30 mins at room temperature, the supernatant was removed, and the precipitate was resuspended in milli-Q water at desired concentration with mild vortexing.

Functionalization of AuNPs with Designed ssDNA (Au-ssDNA): Citrate-stabilized gold nanoparticles ($\approx 3 \times 10^{10}$ particles mL^{-1}) were treated with a 10 μM concentration of single-stranded oligonucleotide (ssDNA). The mixture was stirred for 30 min at room temperature. The solution was then centrifuged, the supernatant discarded to remove the uncapped ssDNA and the pellet was resuspended in milli-Q water at the desired concentration. This was used immediately in experiments. The solutions were nomenclature as Au-ssDNA1a, Au-ssDNA1b, Au-ssDNA2a, Au-ssDNA2b, Au-ssDNA3a, Au-ssDNA3b, Au-ssDNA4a and Au-ssDNA4b. The pair of nanoparticles were then mixed in equal volumes and named Au-ssDNA1, Au-ssDNA2, Au-ssDNA3, and Au-ssDNA4. The nanoparticles were kept at 4 $^{\circ}\text{C}$ for future use.

Synthesis of Graphene Oxide (GO) and Reduced Graphene Oxide (rGO): The synthesis of graphene oxide and reduced graphene oxide was followed using a previously published literature protocol.^[63,64] The

synthesis was carried out from graphite powder by a modified Hummers method as mentioned in the article.

Synthesis of Hafnium Disulfide (HfS₂) Nanoplatelets: The synthesis was carried out following previously reported literature protocol with some modifications.^[65,66] Hafnium chloride (0.73 mmol) and oleylamine (11.2 mmol) were mixed at 300 °C. Carbon disulfide (5.0 mmol) was added to it and the final solution was stirred for about 12 h under constant heating. The product was extracted with excess isopropanol and centrifuged at 10 000 rpm. The supernatant was removed, and the precipitate was washed repeatedly with hexane and methanol. Finally, the purified product, hafnium disulfide, was dried under vacuum and suspended in isopropanol at 0.1 mg mL⁻¹ concentration. The suspension was bath sonicated 4 h prior to use.

Synthesis of Molybdenum Disulfide (MoS₂) Nanoflakes: Molybdenum disulfide (MoS₂) nanoflakes were synthesized following a previously published literature protocol by a simple hydrothermal process.^[67] Sodium molybdate and thiourea were used as precursor reagents for the synthesis.

Synthesis of Covalent Organic Framework (COF): First, 1,3,5-triformylphloroglucinol was synthesized following a previously published literature protocol.^[68] This product was then mixed with 2 equivalent of paraphenylenediamine and a catalytic amount of acetic acid. The mixture was then dissolved in 3:1 v/v mixture of CH₂Cl₂:CHCl₃ and stirred for 48 h at room temperature.^[69] The suspension was centrifuged and washed with dichloromethane twice.

Synthesis of Copper-Embedded Covalent Organic Framework (CuCOF): The as-synthesized COF (10 mg) was mixed with 1 mL of copper chloride (3.08 M) in 20 mL of milli-Q water and stirred for 24 h at room temperature. The products were obtained through centrifugation and washed several times with water.

Absorbance Spectra: The absorbance spectra were acquired on Biotek Synergy Neo2 microplate reader both for endpoint, and spectral analyses.

Sample Standardization Protocol: We intend to influence the plasmonic response of the nanocomposite after sensing its target analyte. Toward this, we mixed the 2D platelets or flakes with 0D nanoparticles to prepare the nanocomposite formulation. Initially, a definite concentration of AuNPs ($\approx 1.2 \times 10^9$ particles mL⁻¹) was mixed with equal concentration (0.4 mg mL⁻¹) of 2D materials, i.e., GO, rGO, HfS₂, MoS₂, COF, and CuCOF. To optimize the concentration of HfS₂ that is required to obtain the best plasmonic response when aggregated with AuNPs, increasing the concentration of HfS₂ (from 0.1 to 1.1 mg mL⁻¹) was added to a well-dispersed solution of AuNPs. However, when ssDNAs were conjugated to AuNPs, the previously optimized concentration of HfS₂ was not enough to provide the optimum agglomeration among the nanoparticles. Hence, the standardization was further performed with increasing concentration of HfS₂ (from 0.2 to 3.6 mg mL⁻¹) added to a fixed concentration of Au-ssDNA ($\approx 1.2 \times 10^9$ particles mL⁻¹). To identify the best pair of oligonucleotides that can selectively detect the complementary strands of the monkeypox virus with the highest efficiency, the nanocomposites (i.e., a mixture of Au-ssDNA and 3.0 mg mL⁻¹ of HfS₂) were added with an equivalent concentration of genomic DNA of monkeypox virus (0.02 ng μ L⁻¹).

Sensing Parameters: To determine the agglomeration efficiency among 2D and 0D nanomaterials, change in absorbance at 600 nm was monitored. On the other hand, a change in absorbance at 540 nm was recorded while adding the genomic DNA of the monkeypox virus to the optimized suspension of the nanocomposite.

Method for Electromagnetic FDTD Simulation: We performed the electromagnetic simulations using Ansys/Lumerical. The complex refractive index of Au was implemented in Lumerical using Johnson and Christy data,^[70] and the refractive index of HfS₂ was set as 3.00 – 0.06i.^[71] The mesh size for the whole domain was set as 1 nm. The simulation 3D domain was surrounded by perfectly matched layers (PMLs) in all the directions. The wavelength of the excitation light was from $\lambda = 300 - 700$ nm. We used Total-Field Scattered-Field (TFSF) source for the simulation in Lumerical to obtain the absorption and

scattering cross-sections. A frequency-domain field monitor was utilized to obtain the local electric field distribution of the plasmonic system.

Calculation of Limit of Detection: An increasing concentration of genomic DNA of the monkeypox virus was added to a pre-optimized formulation of nanocomposite suspension. The change in absorbance was recorded at 615 nm. The limit of detection was then calculated from the titration curve based on the standard deviation of response (Sy) and slope of the curve (S). The formula used for this calculation was: LOD = 3.3(Sy/S).

Determination of Cross-Reactivity: To determine the selectivity of the optimized oligonucleotide strands (ssDNA4a and ssDNA4b), the nanocomposite formulation was added with 0.02 ng mL⁻¹ concentration of genomic DNA from monkeypox virus, *Chlamydia trachomatis*, *Neisseria gonorrhoeae* bacteria and RNA from SARS-CoV-2 virus. The change in absorbance at 540 nm was observed.

Transmission Electron Microscopy: 20 μ L of each of the nanocomposite's suspensions were drop-casted on a formvar coated copper grid. After 10 min, the excess solutions were removed from the grid, and air-dried. TEM data was collected using a Thermo Scientific Talos F200X G2 (S) TEM operated at 200 kV. STEM-EDS mapping was also done on this instrument using the 4 in-column SDD Super-X detectors. EDS maps were collected for ≈ 5 min at a beam current of 0.12 nA and analyzed using the Thermo Scientific Velox software.

Scanning Electron Microscopy: The nanocomposites before and after the addition of genomic DNA from the monkeypox virus were drop-casted on SEM stubs coated with double-sided carbon tape, air-dried, and then sputter coated with 80% platinum/20% palladium to achieve conductivity. The FEI Nova NanoSEM 450 was then used to monitor the surface topography of each of the samples. The field-emission scanning electron microscopic images were recorded. The respective EDS spectra were also recorded for each of the samples.

X-Ray Diffraction Studies: Further to understand the difference in π -stacking distance influencing the aggregation efficacy among the nanoplatelets in the absence and presence of genomic DNA from the monkeypox virus, X-ray diffraction studies were performed in a Bragg-Brentano instrument.

Theoretical Calculations: The nanocomposites (i.e., HfS₂ nanoplatelet; ssDNA4a and ssDNA4b conjugated AuNPs; ssDNA4a and ssDNA4b conjugated AuNPs mixed with HfS₂ nanoplatelet before and after the addition of MPXV DNA) were first energy minimized and then calculated for their HOMO-LUMO orbital energy gaps using GAMESS software. Density functional theoretical (DFT) calculations were performed using MINI basis set, Grid method and B3LYP (Becke-Slater-HF exchange and LYP+VWN5 correlation) functional. Molecular orbitals were calculated using Huckel method.

Method for SERS Imaging: Raman microscopic images of the composite material alone and in presence of the target MPXV DNA and non-target *Neisseria gonorrhoeae* (NG) DNA were collected using Renishaw inVia Reflex Raman Spectroscopy system with the following parameters: 785 nm laser, 45 mW (50%) power, grating of 1200, 100X magnification, acquisition time 0.3 s with the center of Raman frequency set at 1100 cm⁻¹. For the composite material alone, a total of 416 Raman spectra were collected (X = 16 spectra; Y = 26 spectra) with a spatial resolution of 200 nm. For the composite material added with target MPXV DNA, a total of 3036 Raman spectra were collected (X = 46 spectra; Y = 66 spectra) and for the composite material added with non-target NG DNA a total of 1296 Raman spectra were collected (X = 36 spectra; Y = 36 spectra). All spectra were collected with the same spatial resolution of 200 nm along X and Y-directions.

Supporting Information

Supporting Information is available from the Wiley Online Library or from the author.

Acknowledgements

M.I., D.S., P.P., and E.S. contributed equally to this work. The authors gratefully acknowledge the receipt of funding from the University of Maryland Baltimore and The Pennsylvania State University toward the completion of this work. D.P. acknowledge the funding received from Centers for Disease Control and Prevention (Award no. 75D30122C15492), National Science Foundation (Award no. CBET 2153091/2229986) and Department of Defense (DoD) Congressionally Directed Medical Research Program (CDMRP) no. TP210376. M.R.G. acknowledge the support from National Science Foundation (NSF CAREER award number: 2045640). The authors also acknowledge BEI Resources, NIAID, and NIH for providing the genomic DNA from Monkeypox Virus, USA-2003, NR-4928.

Conflict of Interest

The authors declare no conflict of interest.

Data Availability Statement

The data that support the findings of this study are available from the corresponding author upon reasonable request.

Keywords

gold nanoparticles, hafnium disulfide nanoplatelets, H-type aggregation, molecular sensing of MPXV, plasmonic responses, self-assemblies, targeted nucleotide sequences

Received: October 29, 2022

Revised: January 25, 2023

Published online:

- [1] J. R. Kugelman, S. C. Johnston, P. M. Mulembakani, N. Kisalu, M. S. Lee, G. Koroleva, S. E. McCarthy, M. C. Gestole, N. D. Wolfe, J. N. Fair, B. S. Schneider, L. L. Wright, J. Huggins, C. A. Whitehouse, E. O. Wemakoy, J. J. Muyembe-Tamfum, L. E. Hensley, G. F. Palacios, A. W. Rimoin, *Emerg. Infect. Dis.* **2014**, *20*, 232.
- [2] E. Alakunle, U. Moens, G. Nchinda, M. I. Okeke, *Viruses* **2020**, *12*, 1257.
- [3] R. A. Okyay, E. Bayrak, E. Kaya, A. R. Sahin, B. F. Kocyigit, A. M. Tasdogan, A. Avcı, H. E. Sumbul, *Eurasian J Med Oncol* **2022**, *6*, 95.
- [4] J. P. Thornhill, S. Barkati, S. Walmsley, J. Rockstroh, A. Antinori, L. B. Harrison, R. Palich, A. Nori, I. Reeves, M. S. Habibi, V. Apea, C. Boesecke, L. Vandekerckhove, M. Yakubovsky, E. Sendagorta, J. L. Blanco, E. Florence, D. Moschese, F. M. Maltez, A. Goorhuis, V. Pourcher, P. Migaud, S. Noe, C. Pintado, F. Maggi, A.-B. E. Hansen, C. Hoffmann, J. I. Lezama, C. Mussini, A. Cattelan, et al, *N. Engl. J. Med.* **2022**, *387*, 679.
- [5] M. Kozlov, *Nature* **2022**, *608*, 655.
- [6] Y. Xiang, A. White, *Emerg Microbes Infect* **2022**, *11*, 1768.
- [7] E. J. Tarín-Vicente, A. Alemany, M. Agud-Dios, M. Ubals, C. Suñer, A. Antón, M. Arando, J. Arroyo-Andrés, L. Calderón-Lozano, C. Casañ, J. M. Cabrera, P. Coll, V. Descalzo, M. D. Folgueira, J. N. García-Pérez, E. Gil-Cruz, B. González-Rodríguez, C. Gutiérrez-Collar, Á. Hernández-Rodríguez, P. López-Roa, M. de los Ángeles Meléndez, J. Montero-Menárguez, I. Muñoz-Gallego, S. I. Palencia-Pérez, R. Paredes, A. Pérez-Rivilla, M. Piñana, N. Prat, A. Ramirez, Á. Rivero, et al, *Lancet* **2022**, *400*, 661.
- [8] Y. Li, V. A. Olson, T. Laue, M. T. Laker, I. K. Damon, *J. Clin. Virol.* **2006**, *36*, 194.
- [9] I. de Baetselier, C. van Dijk, C. Kenyon, J. Coppens, J. Michiels, T. de Block, H. Smet, S. Coppens, F. Vanroye, J. J. Bugert, P. Girt, S. Zange, L. Liesenborghs, I. Brosius, J. van Griensven, P. Selhorst, E. Florence, D. van den Bossche, K. K. Ariën, A. M. Rezende, K. Vercauteren, M. van Esbroeck, K. Ramadan, T. Platteau, K. van Looveren, J. Baeyens, C. van Hoyweghen, M. Mangelschots, L. Heyndrickx, A. Hauner, et al, *Nat. Med.* **2022**, *28*, 2288.
- [10] K. Brown, P. Leggat, *Trop Med Infect Dis* **2016**, *1*, 8.
- [11] N. Sklenovská, M. van Ranst, *Front Public Health* **2018**, *6*, 241.
- [12] M. Ahmed, H. Naseer, M. Arshad, A. Ahmad, *Ann. Med. Surg.* **2022**, *78*, 103975.
- [13] P. L. Earl, J. L. Americo, L. S. Wyatt, L. Anne Eller, D. C. Montefiori, R. Byrum, M. Piatak, J. D. Lifson, R. Rao Amara, H. L. Robinson, J. W. Huggins, B. Moss, *Virology* **2007**, *366*, 84.
- [14] K. J. Stittelaar, G. van Amerongen, I. Kondova, T. Kuiken, R. F. van Lavieren, F. H. M. Pistor, H. G. M. Niesters, G. van Doornum, B. A. M. van der Zeijst, L. Mateo, P. J. Chaplin, A. D. M. E. Osterhaus, *J. Virol.* **2005**, *79*, 7845.
- [15] I. Srivastava, S. K. Misra, F. Ostadhossein, E. Daza, J. Singh, D. Pan, *Nano Res.* **2017**, *10*, 3269.
- [16] F. Ostadhossein, D. Pan, *WIREs Nanomed. Nanobiotechnol.* **2017**, *9*, e1436.
- [17] L. Cappelli, P. Cinelli, F. Giusti, I. Ferlenghi, S. Utrio-Lanfalconi, N. Wahome, M. J. Bottomley, D. Maione, R. Cozzi, *PLoS One* **2022**, *17*, e0273322.
- [18] M. H. Ross, A. K. Esser, G. C. Fox, A. H. Schmieder, X. Yang, G. Hu, D. Pan, X. Su, Y. Xu, D. v. Novack, T. Walsh, G. A. Colditz, G. H. Lukaszewicz, E. Cordell, J. Novack, J. A. J. Fitzpatrick, D. L. Waning, K. S. Mohammad, T. A. Guise, G. M. Lanza, K. N. Weilbaeher, *Cancer Res.* **2017**, *77*, 6299.
- [19] P. Fathi, H. J. Knox, D. Sar, I. Tripathi, F. Ostadhossein, S. K. Misra, M. B. Esch, J. Chan, D. Pan, *ACS Nano* **2019**, *13*, 7690.
- [20] H. Gleiter, *Acta Mater.* **2000**, *48*, 1.
- [21] S. Yadav, A. K. Sharma, P. Kumar, *Front Bioeng Biotechnol* **2020**, *8*.
- [22] M. S. Khan, S. K. Misra, K. Dighe, Z. Wang, A. S. Schwartz-Duval, D. Sar, D. Pan, *Biosens. Bioelectron.* **2018**, *110*, 132.
- [23] I. Srivastava, J. S. Khamo, S. Pandit, P. Fathi, X. Huang, A. Cao, R. T. Haasch, S. Nie, K. Zhang, D. Pan, *Adv. Funct. Mater.* **2019**, *29*, 1902466.
- [24] D. Pan, C. T. N. Pham, K. N. Weilbaeher, M. H. Tomasson, S. A. Wickline, G. M. Lanza, *WIREs Nanomed. Nanobiotechnol.* **2016**, *8*, 85.
- [25] M. S. Khan, K. Dighe, Z. Wang, I. Srivastava, E. Daza, A. S. Schwartz-Dual, J. Ghannam, S. K. Misra, D. Pan, *Analyst* **2018**, *143*, 1094.
- [26] S. K. Misra, F. Ostadhossein, E. Daza, E. v. Johnson, D. Pan, *Adv. Funct. Mater.* **2016**, *26*, 8031.
- [27] M. L. Becker, H. Fang, X. Li, D. Pan, R. Rossin, X. Sun, J.-S. Taylor, J. L. Turner, M. J. Welch, K. L. Wooley, *WO2006044716A3* **2013**.
- [28] S. K. Misra, H.-H. Chang, P. Mukherjee, S. Tiwari, A. Ohoka, D. Pan, *Sci. Rep.* **2015**, *5*, 14986.
- [29] S. K. Ghosh, A. Böker, *Macromol. Chem. Phys.* **2019**, *220*, 1900196.
- [30] M. Alafeef, K. Dighe, P. Moitra, D. Pan, *ACS Nano* **2020**, *14*, 17028.
- [31] P. Moitra, D. Bhagat, V. B. Kamble, A. M. Umarji, R. Pratap, S. Bhattacharya, *Biosens. Bioelectron.* **2021**, *173*, 112728.
- [32] C. Zhang, B. Xie, Y. Zou, D. Zhu, L. Lei, D. Zhao, H. Nie, *Adv Drug Deliv Rev* **2018**, *132*, 33.
- [33] Z. Wang, T. Hu, R. Liang, M. Wei, *Front Chem* **2020**, *8*, 320.

- [34] S. Pedireddy, H. K. Lee, W. W. Tjiu, I. Y. Phang, H. R. Tan, S. Q. Chua, C. Troadec, X. Y. Ling, *Nat. Commun.* **2014**, *5*, 4947.
- [35] M. T. Gole, Z. Yin, M. C. Wang, W. Lin, Z. Zhou, J. Leem, S. Takekuma, C. J. Murphy, S. Nam, *Sci. Rep.* **2021**, *11*, 12232.
- [36] W. Lee, Y. Liu, Y. Lee, B. K. Sharma, S. M. Shinde, S. D. Kim, K. Nan, Z. Yan, M. Han, Y. Huang, Y. Zhang, J.-H. Ahn, J. A. Rogers, *Nat. Commun.* **2018**, *9*, 1417.
- [37] K. Kneipp, Y. Wang, H. Kneipp, L. T. Perelman, I. Itzkan, R. R. Dasari, M. S. Feld, *Phys. Rev. Lett.* **1997**, *78*, 1667.
- [38] S. Nie, S. R. Emory, *Science* **1997**, *275*, 1102.
- [39] M. Alafeef, P. Moitra, K. Dighe, D. Pan, *ACS Nano* **2021**, *15*, 13742.
- [40] M. Alafeef, P. Moitra, K. Dighe, D. Pan, *Nat. Protoc.* **2021**, *16*, 3141.
- [41] P. Moitra, M. Alafeef, K. Dighe, D. Pan, *Biosens. Bioelectron.* **2022**, *207*, 114718.
- [42] Z. Sheffield, M. Alafeef, P. Moitra, P. Ray, D. Pan, *Nanoscale* **2022**, *14*, 5112.
- [43] K. Kumar, P. Moitra, M. Bashir, P. Kondaiah, S. Bhattacharya, *Nanoscale* **2020**, *12*, 1067.
- [44] K. Dighe, P. Moitra, M. Alafeef, N. Gunaseelan, D. Pan, *Biosens. Bioelectron.* **2022**, *200*, 113900.
- [45] P. Moitra, M. Alafeef, K. Dighe, M. B. Frieman, D. Pan, *ACS Nano* **2020**, *14*, 7617.
- [46] P. Moitra, M. Alafeef, K. Dighe, Z. Sheffield, D. Dahal, D. Pan, *Chem. Commun.* **2021**, *57*, 6229.
- [47] P. Moitra, A. Chaichi, S. M. Abid Hasan, K. Dighe, M. Alafeef, A. Prasad, M. R. Gartia, D. Pan, *Biosens. Bioelectron.* **2022**, *208*, 114200.
- [48] P. Moitra, M. Alafeef, K. Dighe, P. Ray, J. Chang, A. Thole, B. Punshon-Smith, M. Tolosa, S. S. Ramamurthy, X. Ge, D. D. Frey, D. Pan, G. Rao, *Biotechnol. Bioeng.* **2021**, *118*, 3029.
- [49] H. Li, X. Wang, *Sci China Chem* **2015**, *58*, 1792.
- [50] R. Khan, A. Radoi, S. Rashid, A. Hayat, A. Vasilescu, S. Andreescu, *Sensors* **2021**, *21*, 3369.
- [51] J. Pradhan, P. Moitra, Umesh, B. D. , P. Mondal, G. S. Kumar, U. K. Ghorai, S. Acharya, S. Bhattacharya, *Chem. Mater.* **2020**, *32*, 7159.
- [52] T. Li, W. Yin, S. Gao, Y. Sun, P. Xu, S. Wu, H. Kong, G. Yang, G. Wei, *Nanomaterials* **2022**, *12*, 982.
- [53] X. Huang, M. A. El-Sayed, *J. Adv. Res.* **2010**, *1*, 13.
- [54] S. Lee, K. Sim, S. Y. Moon, J. Choi, Y. Jeon, J. Nam, S. Park, *Adv. Mater.* **2021**, *33*, 2007668.
- [55] J. R. Weaver, S. N. Isaacs, *Immunol. Rev.* **2008**, *225*, 96.
- [56] J. R. Kugelman, S. C. Johnston, P. M. Mulembakani, N. Kisalu, M. S. Lee, G. Koroleva, S. E. McCarthy, M. C. Gestole, N. D. Wolfe, J. N. Fair, B. S. Schneider, L. L. Wright, J. Huggins, C. A. Whitehouse, E. O. Wemakoy, J. J. Muyembe-Tamfum, L. E. Hensley, G. F. Palacios, A. W. Rimoin, *Emerg. Infect. Dis.* **2014**, *20*, 232.
- [57] Y. Yuan, J. Shu, P. Liu, Y. Zhang, Y. Duan, J. Zhang, *J. Phys. Chem. B* **2015**, *119*, 8446.
- [58] S. Bhattacharjee, S. K. Samanta, P. Moitra, K. Pramoda, R. Kumar, S. Bhattacharya, C. N. R. Rao, *Chemistry* **2015**, *21*, 5467.
- [59] P. Moitra, *Bioorg. Chem.* **2019**, *86*, 15.
- [60] S. K. Misra, P. Moitra, P. Kondaiah, S. Bhattacharya, *Colloids Surf. B Biointerfaces* **2016**, *142*, 130.
- [61] D. Sar, F. Ostadhossein, P. Moitra, M. Alafeef, D. Pan, *Advanced Science* **2022**, *9*, 2270138.
- [62] Y. Ding, C. Y. Chan, C. E. Lawrence, *Nucleic Acids Res.* **2004**, *32*, W135.
- [63] W. S. Hummers, R. E. Offeman, *J. Am. Chem. Soc.* **1958**, *80*, 1339.
- [64] J. Jo, S. Lee, J. Gim, J. Song, S. Kim, V. Mathew, M. H. Alfaruqi, S. Kim, J. Lim, J. Kim, *R. Soc. Open Sci.* **2019**, *6*, 181978.
- [65] S. Jeong, D. Yoo, J. Jang, M. Kim, J. Cheon, *J. Am. Chem. Soc.* **2012**, *134*, 18233.
- [66] S. H. Chae, Y. Jin, T. S. Kim, D. S. Chung, H. Na, H. Nam, H. Kim, D. J. Perello, H. Y. Jeong, T. H. Ly, Y. H. Lee, *ACS Nano* **2016**, *10*, 1309.
- [67] S. Wang, G. Li, G. Du, X. Jiang, C. Feng, Z. Guo, S.-J. Kim, *Chin. J. Chem. Eng.* **2010**, *18*, 910.
- [68] J. H. Chong, M. Sauer, B. O. Patrick, M. J. MacLachlan, *Org. Lett.* **2003**, *5*, 3823.
- [69] Y. Shi, S. Liu, Z. Zhang, Y. Liu, M. Pang, *Chem. Commun.* **2019**, *55*, 14315.
- [70] P. B. Johnson, R. W. Christy, *Phys. Rev. B* **1972**, *6*, 4370.
- [71] X. F. Yue, Y. Liang, J. Jiang, R. G. Liu, S. T. Ren, R. X. Gao, B. Zhong, G. W. Wen, Y. Y. Wang, M. Q. Zou, *Nanoscale* **2019**, *11*, 2179.